Offline impact of transcranial focused ultrasound on cortical activation in primates

Lennart Verhagen[1,2,8*], Cécile Gallea[3,8], Davide Folloni[1,2], Charlotte Constans[4], Daria EA Jensen[1,2], Harry Ahnine[3], Léa Roumazeilles[1,2], Mathieu D Santin[3], Bashir Ahmed[5], Stéphane Lehericy[3], Miriam Klein-Flügge[1,2], Kristine Krug[5], Rogier B Mars[2,6], Matthew FS Rushworth[1,2,8], Pierre Pouget[7,8], Jean-François Aubry[4,8], Jérôme Sallet[1,2,8*]

[1] Wellcome Centre for Integrative Neuroimaging (WIN), Department of Experimental Psychology, University of Oxford, Oxford, OX1 3SR, UK
[2] Wellcome Centre for Integrative Neuroimaging (WIN), Centre for Functional MRI of the Brain (FMRIB), Nuffield Department of Clinical Neurosciences, John Radcliffe Hospital, University of Oxford, Oxford, OX3 9DU, UK
[3] Institute du Cerveau et de la Moelle épinière (ICM), Centre for NeuroImaging Research (CENIR), Inserm U 1127, CNRS UMR 7225, Sorbonne Université, F-75013, Paris, France
[4] Institut Langevin, ESPCI Paris, PSL Research University, CNRS 7587, INSERM U979, Sorbonne Université, Paris, France
[5] Department of Physiology, Anatomy, and Genetics, University of Oxford, Oxford, OX1 3PT, UK
[6] Donders Institute for Brain, Cognition and Behaviour, Radboud University Nijmegen, 6525 HR, Nijmegen, the Netherlands
[7] Institute du Cerveau et de la Moelle épinière (ICM), UMRS 975 INSERM, CNRS 7225, UMPC, Paris, France
[8] These authors contributed equally

[*] To whom correspondence should be addressed

Name: Lennart Verhagen, Jérôme Sallet
E-mail: lennart.verhagen@psy.ox.ac.uk, jerome.sallet@psy.ox.ac.uk
Phone: 0044 1865 612737, 0044 1865 671418
Address: Lennart Verhagen, Jérôme Sallet
Department of Experimental Psychology,
University of Oxford,
Tinsley Building,
Mansfield Road,
Oxford,
OX1 3SR, UK

Keywords: brain stimulation, transcranial focused ultrasound, neuroimaging, resting-state fMRI, connectivity, frontal lobe

Abstract

To understand brain circuits it is necessary both to record and manipulate their activity. Transcranial ultrasound (TUS) is a promising non-invasive brain stimulation technique. To date, investigations have focused on short-lived neuromodulatory effects, but to deliver on its full potential for research and therapy, ultrasound protocols are required that induce longer-lasting 'offline' changes. Here, we present a TUS protocol that modulates brain activation in macaques for more than one hour after 40 seconds of stimulation, while circumventing auditory confounds. Normally activity in brain areas reflects activity in interconnected regions but TUS' impact can be demonstrated by showing such patterns change for stimulated areas. We report regionally specific TUS effects for two medial frontal brain regions – supplementary motor area and frontal polar cortex. Independently of these site-specific effects, TUS also induced signal changes in the meningeal compartment. TUS effects were temporary and not associated with microstructural changes.

Introduction

In neuroscience, to understand brain circuits a two-pronged approach, entailing both recording and manipulating brain activity, is essential. In recent years, there has been extensive progress in this field, which was in part made possible by the availability of new technologies[1–3]. While techniques for transiently manipulating activity in rodents, such as microstimulation, optogenetics, and chemogenetics[4,5], are increasingly accessible and applied, techniques for manipulating activity in the primate brain are less widely available and remain accessible to comparatively few researchers in a limited number of research centers worldwide[5–7]. A prominent limitation for many brain stimulation tools for research and therapeutic interventions is the duration of the induced neuromodulatory effects, often not outlasting the stimulation by more than a few seconds or minutes.

Here we report on a particular protocol of low intensity transcranial focused ultrasound stimulation (TUS) that we show induces a sustained period of neuromodulation without inducing structural damage. The TUS approach in general is a relatively new one[8–12] and like transcranial magnetic stimulation[2] and transcranial electric stimulation[3] it can be applied in the absence of a craniotomy. *In vitro* recordings have identified several mechanisms by which ultrasound stimulation could affect neurons. It has been proposed that the sound pressure wave exerts a mechanical effect on neuronal activity through ion channel gating[13–15]. In the macaque, its application over the frontal eye field (FEF) affects the same aspects of oculomotor behavior that are compromised by FEF lesion, whilst leaving intact those aspects of oculomotor behavior that are unaffected by FEF lesion[16]. Recent work has highlighted the possibility that in rodents some TUS protocols can evoke a startle response when the stimulation is modulated at audible frequencies[17,18]. Importantly, this auditory effect is limited to the stimulation period and dissipates within 75 ms to 4 s. This work has also emphasized that in more deeply anaesthetized animals, when the intrinsic neural activity of a system is suppressed, some TUS protocols might fail to evoke action potentials at the site

of stimulation. This suggests TUS' actions might be primarily neuromodulatory in nature and/or that they are most prominently observable when they interact with ongoing physiological activity. However, as has been noted[19] the impact that any stimulation protocol might have, will be a function of the animal model being used and the precise details of the ultrasound frequencies, pulse shape, protocol, and ongoing brain activity. With the offline protocol and anesthesia regime we used we control for such potential artefacts and show that TUS has an effect that cannot be attributed to them.

Here we focused on the effects of TUS outlasting the stimulation period, investigating the impact of 40 s trains of TUS on measurements of neural activity provided by functional magnetic resonance imaging (fMRI) up to 2 hours after stimulation. FMRI is one of the most widely used methods for estimating neural activity. Despite limitations in its spatial and temporal resolution, fMRI remains important because it is non-invasive and can often be used to provide information about activity throughout the whole brain. Rather than providing a direct measure of neural activity, however, it provides an estimate of how activity changes in tandem with sensory, cognitive, or motor events or with activity in another brain region. Typically, fMRI-measured activity in any given brain area is a function of activity in other brain areas especially those with which it is closely interconnected[20,21]. Although many brain areas may share any given individual connection (for example both areas A and B may project to C), the overall pattern of connections of each area is unique[22]; as such, the overall pattern of connections therefore constitutes a 'connectional fingerprint'. As a result it is possible to use fMRI measurements of correlations in the blood oxygen level dependent (BOLD) signal across brain regions to estimate the connectivity fingerprints of a given brain area[23–30]. This implies that activity in any given brain area is a function of the activity in the areas with which it is interconnected.

We exploited this feature of activity to examine the impact of TUS application to two brain regions in the frontal cortex: supplementary motor area (SMA; experiment 1) and frontal polar cortex (FPC; experiments 2 and 3). Simulations showed we were able to

selectively target these regions (Fig. 1c,f; see *Acoustic and thermal modelling* for more details). These regions have distinct anatomical and functional connections; SMA is most strongly coupled with the sensorimotor system, while the FPC interacts primarily with the prefrontal cortex and only interacts indirectly with the sensorimotor system via SMA[28,31]. This allows us to test the spatial and connectional specificity of TUS effects. In the control state, each area's activity is normally a function of the activity in the areas that constitute its connectional fingerprint. If this pattern is altered by TUS in a manner that is dependent on the location of the stimulation, then this will constitute evidence that TUS exerts a spatially selective effect on neural activity. The same three animals participated in experiments 1 and 2, and a control experiment conducted in the absence of TUS. We also validated the results of experiment 2 in a new set of three different animals (experiment 3).

Ultrasound modulation of SMA and FPC led to focal, area-specific changes in each stimulated region's connectivity profile. In each area, a region's activity pattern after TUS application was more a function of its own activity and that of strongly connected regions, but less a function of activity in more remote and weakly interconnected areas. Independent of these specific gray matter signal changes, TUS also interacted with non-neuronal structures, as evidenced by more widespread signal changes observed in the meningeal compartment (including cerebral spinal fluid and vasculature). Finally, in experiment 4 we demonstrate that TUS application had no observable impact on cortical microstructure apparent on histological examination. In summary, TUS over dorsomedial frontal cortex causes spatially specific sharpening of the stimulated region's connectivity profile with high efficacy and reproducibility, independent of non-neuronal signal changes.

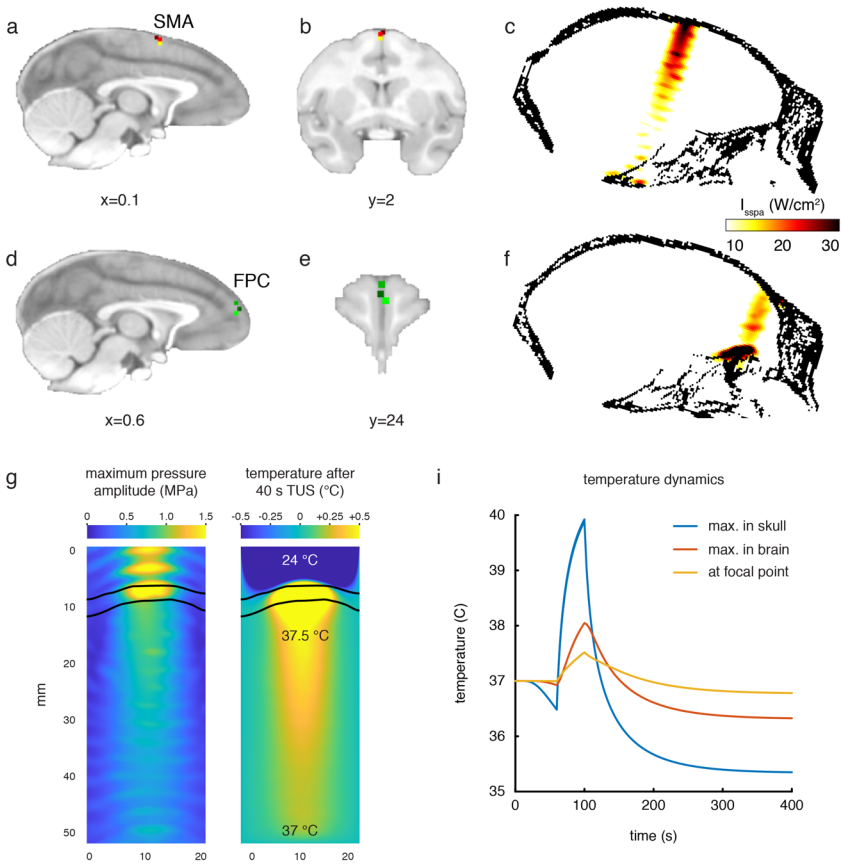

Fig. 1. Stimulation targets and thermal modelling. Stimulation target position is shown in each of three individual animals in three different colors in SMA on sagittal (**a**) and coronal views (**b**). (**c**) Estimates of the focused ultrasound peak intensities and spatial distribution when targeting SMA are derived from numerical simulations using a high-resolution macaque whole-head CT scan. FPC targets in three animals are shown on sagittal (**d**) and coronal sections (**e**). (**f**) Estimated peak intensities and spatial distribution when targeting FPC. (**g**) Whole-head simulations of the acoustic wave and thermal dynamics provided estimates of the maximum pressure amplitude (left panel) and the temperature after 40 s TUS (right panel). The data in panels g depicts a cropped plane of the whole-head simulations with the sonic coupling cone at the top and the brain at the bottom; the skull is outlined in black. Pressure and temperature are maximal in the skull, which is more absorbing than soft tissue. (**i**) Temperature dynamics for the maximum temperature in the skull (blue), maximum temperature in the brain (red) and at the geometrical focal point in the cortex (yellow).

Results

Experiment 1, TUS modulation of SMA connectivity

Transcranial focused ultrasound stimulation of SMA induced spatially specific changes to the connectivity profile that SMA has even at rest. At rest, in the control state, SMA's activity is coupled with activity throughout sensorimotor regions in frontal and parietal cortex, inferior parietal, prefrontal, and parts of cingulate cortex (Fig. 2a). Many of these regions are anatomically connected with SMA[32–34]. If we change the responsiveness of SMA neurons to such activity in interconnected regions by artificially modulating SMA activity with TUS then we should see a change in the coupling between SMA activity and activity in other regions. Following ultrasound stimulation, SMA changed its coupling with the sensorimotor system, anterior and posterior cingulate, anterior temporal, inferior parietal, and prefrontal cortex (Fig. 2b). This can be seen on the whole brain functional connectivity maps for the SMA region highlighted by the dashed black circles on the left column of panels in Fig. 2 (compare panels a and b).

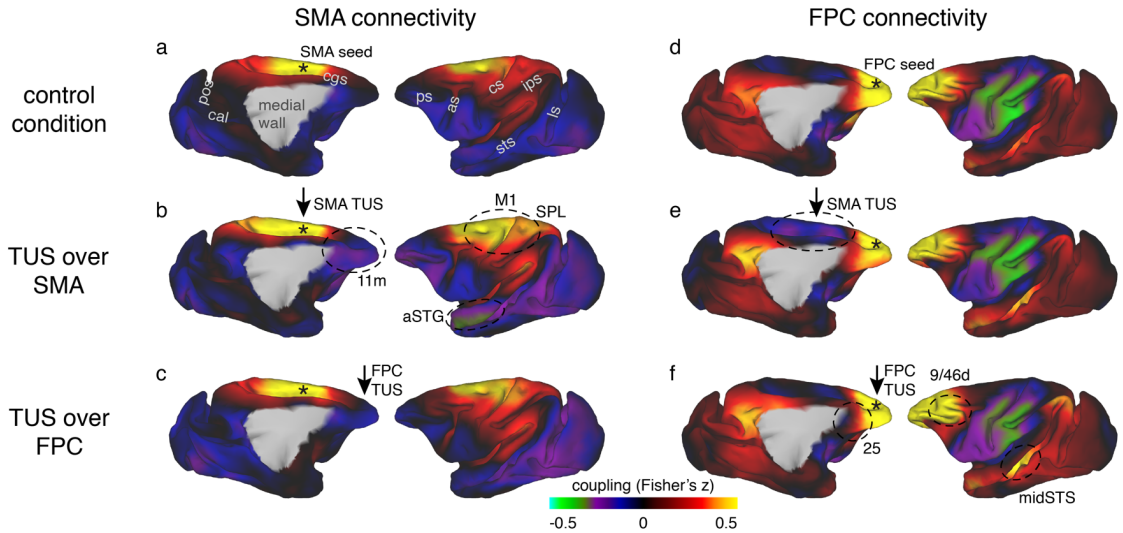

Fig. 2. Coupling of activity between stimulated areas and the rest of the brain in experiments 1 (SMA) and 2 (FPC). The left panels show activity coupling between SMA and the rest of the brain in control animals (**a**), after

SMA TUS (**b**), and after FPC TUS (**c**). The right panels show activity coupling between FPC and the rest of the brain in control animals (**d**), after SMA TUS (**e**), and after FPC TUS (**f**). Functional connectivity from TUS-targeted regions is therefore summarized in panels (**b**) and (**f**) (i.e. SMA connectivity after SMA TUS and FPC connectivity after FPC TUS). Each type of TUS had a relatively selective effect on the stimulated area: SMA coupling was changed by SMA TUS (**b**) and FPC coupling was changed by FPC TUS (**f**). Positive correlations represented in warm colors from red to yellow, negative correlations represented in cool colors from blue to green. Key regions of change are highlighted by black dashed ovals. TUS target sites are indicated with arrows. Connectivity seed regions are indicated with black asterisks. Key anatomical features are labelled in panel (**a**): pos, parieto-occipital sulcus; cal, calcarine sulcus; cgs, cingulate sulcus; ps, principal sulcus; as, arcuate sulcus; cs, central sulcus; ips, intraparietal sulcus; sts, superior temporal sulcus; ls, lunate sulcus.

It is also apparent in the illustration of SMA's connectional fingerprint (Fig. 3a). The distance of each colored line from the center of the figure (and hence its proximity to the circumference of the figure) indicates the strength of activity coupling between SMA and each of the other brain areas indicated on the circumference in the control state. Compared to the control state (blue line), after TUS over SMA (red line) SMA's positive coupling is enhanced with proximal areas in the sensorimotor system but reduced in many long-range connections after SMA TUS (non-parametric permutation test, p=0.017). The primary motor cortex (M1), superior parietal lobe (SPL), and middle cingulate cortex (MCC) in the dorsomedial sensorimotor network have been reported to be closely connected with the SMA, whereas prefrontal regions on the dorsomedial (area 9m and FPC), dorsolateral (areas 9-46d and 8A), and ventromedial (area 11m) surface, and those in the temporal lobe (anterior superior temporal gyrus, aSTG; middle superior temporal sulcus, midSTS), and parietal cortex (caudal inferior parietal lobule, IPLc; posterior parietal cortex, PCC) have been reported to be less closely connected with the SMA[32–34]. TUS increased positive coupling between the stimulated area and proximal areas normally closely connected with it while, at the same time, decreasing coupling between the stimulated area and many areas normally less closely connected with it.

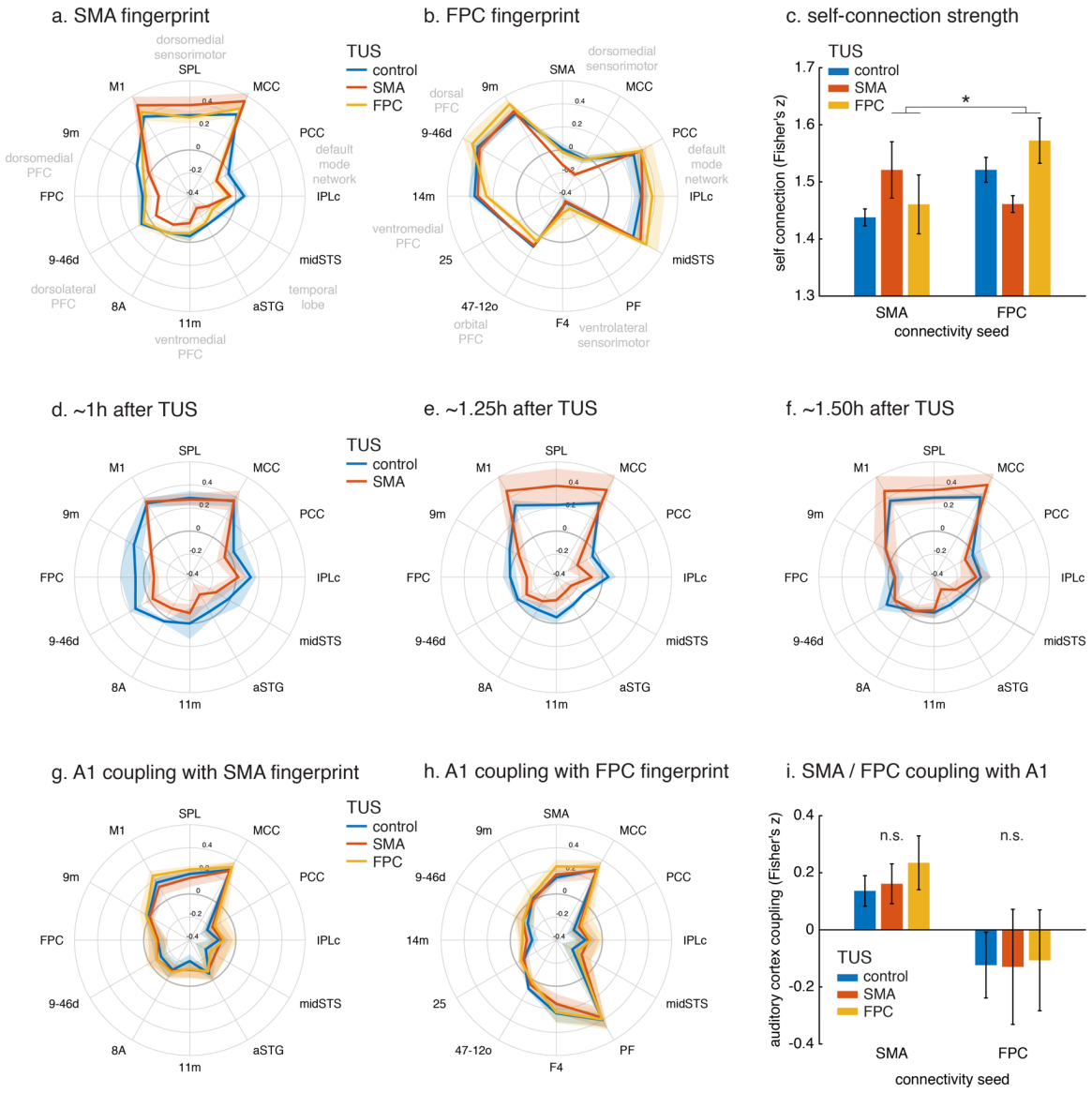

Fig. 3. Connectional fingerprints of the stimulated areas. Fingerprint target regions were drawn from the literature and chosen based on their known and distinct connectivity, either strong or weak, with the seed region. Activity coupling in the control state is indicated in blue, following SMA TUS in red, and FPC TUS in yellow. (**a**) SMA connectional fingerprint. In the control state (blue) SMA is strongly coupled to areas in the dorsomedial sensorimotor system (M1, SPL, MCC). Coupling with each of these areas is enhanced after SMA TUS (red). In contrast, coupling with regions that SMA is weakly connected with in the control state are even further reduced after SMA TUS (red). However, SMA's fingerprint is relatively unaffected after FPC TUS (yellow), but some effects

are visible for regions that are strongly coupled with FPC (compare to panel b). (**b**) FPC connectional fingerprint is sharpened following FPC TUS, but not following SMA TUS. The latter only affected coupling with SMA itself and regions strongly connected to it (MCC). (**c**) TUS induced more homogenous activity within the stimulated area (SMA in red on the left, FPC in yellow on the right). (**d-f**) Temporal evolution of the effect of SMA TUS on the SMA connectional fingerprint. The left panels depict effects observed in the first fMRI run, followed by the second run in the middle, and the third and last run on the right. For each run, the time after TUS refers to the duration between the end of TUS and the midpoint of the run, averaged across the 3 animals. (**g-h**) TUS-induced effects on the connectional fingerprints of SMA and FPC could not be explained by auditory activity. (**i**) There were no changes in the coupling between the stimulation sites and auditory cortex. In all plots, thick lines and histograms indicate mean activity coupling; lighter colored error bands and error bars depict standard-error of the mean; asterisk denotes the interaction between TUS and connectivity seed ($p < 0.001$).

These specific effects of TUS were sustained over the duration of our experiment, lasting up to 2 hours (Fig. 3d-f). Disruptive effects of TUS on long-range coupling were especially prominent immediately following the end of TUS application (Fig. 3d), and gradually reduced towards the end of our recording session (Fig. 3f). The enhancing effects that TUS exerted on SMA's coupling with adjacent and strongly connected areas had a relatively delayed appearance, arising well after the TUS had ended (more than 1 hour, Fig. 3e), but again decreasing towards the end of the recording session.

Experiment 2, TUS modulation of FPC connectivity

Like SMA, FPC's activity is coupled with that in interconnected brain regions even when animals are at rest in the control state (Fig. 2d). FPC's activity is positively correlated with activity in a number of adjacent dorsomedial and lateral prefrontal areas and in the central portion of the superior temporal sulcus (midSTS) and posterior cingulate cortex with which it is monosynaptically interconnected[31]. By contrast there was, at a rest, a negative relationship with the activity in sensorimotor areas with which it is indirectly connected via regions such as SMA.

In comparison to the control state FPC stimulation induced an enhancement in the normal short-range connectivity between FPC and adjacent dorsomedial (area 9m) and lateral prefrontal cortex (area 9-46d) with which it is particularly strongly connected. In addition, a similar effect was seen in more distant regions with which it is also strongly connected – the midSTS, IPLc and PCC, together comprising temporal and parietal segments of the primate 'default mode network'[31]. By contrast, there was reduced coupling with other areas in prefrontal cortex, including ventromedial (area 14m), subgenual cingulate (area 25), and lateral orbitofrontal cortex (area 47-12o). These are all areas that FPC is connected to but less strongly[31]. Finally, TUS applied to FPC also led to a change in long-range connectivity between FPC and several motor association regions with which it is not directly connected, especially those in the ventrolateral parieto-frontal sensorimotor network (areas PF and F4)[31]. As noted, in the control state, the activity in FPC and these sensorimotor association areas is negatively or anti-correlated, but this anti-correlation was reduced by FPC TUS. These results are apparent in the whole brain functional connectivity maps for the FPC region highlighted by the dashed black circles on the right panels in Fig. 2 (compare panels d and f). It is also apparent in the illustration of FPC's connectional fingerprint (Fig. 3b). Here the blue line indicates the strength of activity coupling between FPC and each of the other brain areas indicated on the circumference in the control state. The yellow line shows that FPC's coupling with each area is changed after FPC TUS (non-parametric permutation test, $p = 0.027$).

Comparing experiments 1 (SMA) and 2 (FPC)

It is important to test the claim that TUS induces effects that are spatially specific to each sonicated area by directly comparing effects between stimulation sites. Although FPC TUS significantly altered FPC functional connectivity, it had comparatively little impact on SMA's pattern of functional connectivity; there was no difference in SMA's functional connectivity between the control state and after FPC TUS (non-parametric permutation test, $p = 0.231$; whole-brain map in Fig. 2c and yellow line in connectivity fingerprint in Fig. 3a). Importantly,

the effects of TUS over SMA on SMA's connectivity were significantly dissociable from the effects of FPC TUS (non-parametric permutation test, $p = 0.041$). Similarly, SMA TUS had some but comparatively little impact on FPC's pattern of functional connectivity (non-parametric permutation tests, SMA versus control, $p = 0.047$; SMA versus FPC, $p = 0.028$; whole-brain map in Fig. 2e and red line in connectivity fingerprint in Fig. 3b). In fact, the most prominent changes in each area's connectional fingerprint that were induced by stimulation of the other area were the disruption of functional connectivity between FPC and sensorimotor areas when SMA was stimulated (Fig. 2e, encircled). This particular result may have occurred because, as already noted, FPC has no direct monosynaptic connections with these sensorimotor areas[31] and so its functional coupling with these areas is likely to be mediated by areas such as SMA and the areas that surround it such as the pre-supplementary motor area and the cingulate motor areas[35,36]. In fact, these circumscribed exceptions may well confirm the rule that a region's connectivity pattern is only affected by stimulation of the region itself. Namely, SMA TUS only affects FPC coupling with SMA itself and the regions which are coupled with FPC only through SMA. In conclusion, the effects of TUS in different frontal regions were clearly dissociable.

Experiment 3, replication of TUS effects on FPC connectivity

We investigated the reproducibility of TUS effects by examining the impact of TUS to FPC in three additional individuals (Supplementary Fig. 1). TUS had the same effects as seen in experiment 2: a site-specific sharpening of the stimulated region's connectional profile. While experiments 1 and 2 followed a within-subject design, for experiment 3 we conducted a between-subject analysis where the subjects in the two experiments differed in age. We are therefore careful not to draw too strong conclusions on any main effect of subject group but focus on the interaction of the TUS effect with the fingerprint shape. Notwithstanding, when reviewing the simple effects driving the well-matched interaction, we note that the observed sharpening was less prominently related to activity coupling decreases in experiment 3 than

in experiment 2. As already mentioned, parameters of the general anaesthesia could impact on the effect of TUS. However, subjects used in experiment 2 and 3 did not differ regarding depth of anaesthesia or duration between sedation and fMRI data collection.

Effects of TUS on activation in the stimulated regions and on the auditory system

It has recently been suggested that certain TUS protocols might have a limited efficacy in evoking spiking activity at the stimulation site, but rather exert their influence on the brain through the auditory system, not unlike an auditory startle response[17,18]. Although these online observations in rodents should perhaps not be extrapolated far outside the tested conditions (for example to our measurements taken tens of minutes after the stimulation ended), these observations do argue in favor of performing controlled experiments that address and exclude such confounds[19]. Here we consider, first, why neural effects of TUS might be evident in the current study when they were not clear previously. Second, we consider whether neural effects may be due to an auditory artefact.

First, it is possible that the efficacy of TUS is a function of both the specifics of the stimulation protocol and of ongoing neural activity. A neuromodulatory technique may fail to elicit spiking activity in deeply anesthetized rodents[17,18]. However, in this study we specifically test whether it simply modulates ongoing activity, while adopting lighter anesthesia levels. Importantly, it is known that whole-brain functional connectivity, as measured with the BOLD signal, is preserved at these levels[20,21,27,28,45,59]. Finally, the experiments were conducted in a primate model as opposed to a rodent model; the importance of species specific effects in TUS models are currently unknown. Under these distinct conditions, we observed that TUS modulated the activity coupling of each stimulated area in a regionally specific manner.

Nevertheless, following these investigations of the effect of TUS on whole-brain connectivity patterns of the stimulated regions, we carried out a second line of investigation and examined the effect of TUS on the signal in the stimulated regions themselves (Fig. 3c). While BOLD fMRI cannot provide an absolute measure of neural activity, we can characterize

how homogeneous the activation signal is within the stimulated region, as quantified by the coupling strength of the signal at each point in the stimulated region of interest to all other points in that region. This analysis revealed that TUS induced more homogenous activation within the stimulated area, but not in the non-stimulated region (interaction of TUS x connectivity seed: $F_{(1,8)}$=1571.2, p=1.8044e-10, d=11.4426, CI=[1.2733 1.1333]).

Third, the presence of auditory and somatosensory confounds is likely to be a function of the specifics of the TUS protocol. For example, auditory stimulation could be expected when ultrasound is modulated at frequencies well within the audible range of rodents[17,18]. This is something that we have avoided in our work with macaques. Moreover, here we adopted an offline experimental design where any potential audible stimulation associated with the TUS application was limited to the 40 s sonication period, while the neural activation measures were initiated tens of minutes later. Furthermore, the specificity of our results strengthens the suggestion that it might not be possible to explain away the current findings as the result of an auditory artefact having occurred up to two hours earlier.

Nevertheless, we also carried out a fourth line of inquiry and examined the activation in the primary auditory cortex (A1) and its relationship with activity in the rest of the brain (Fig. 3g-i). The effects of TUS on SMA and FPC coupling patterns, as quantified in their connectional fingerprints, could not be explained by a potential impact of TUS on A1 activity coupling. In fact, TUS did not affect A1 activity coupling with SMA fingerprint targets (Fig. 3g; non-parametric permutation tests, SMA TUS: p=0.8234, FPC TUS p=0.3452), nor its coupling with FPC fingerprint targets (Fig. 3h; non-parametric permutation tests, SMA TUS: p=0.5411, FPC TUS p=0.2667). Moreover, neither SMA nor FPC changed its coupling with A1 as a function of TUS (Fig. 3i; main effect of TUS: $F_{(1,8)}$=0.015445, p=0.90416, d=0.03583, CI=[-0.41483 0.46209]; interaction of TUS x connectivity seed: $F_{(1,8)}$=0.18284, p=0.68022, d=0.1234, CI=[-0.25058 0.36466]).

Non-neuronal signal changes

The ability of ultrasound to reversibly interact with biological tissue is not limited to gray matter. We were aware that our ultrasonic beam, placed over the central midline to target SMA or FPC in both hemispheres simultaneously, was also likely to reach the meningeal compartment in the interhemispheric fissure. In fMRI analyses this region is sometimes referred to as 'cerebral spinal fluid', although in reality it contains the cortical membranes (dura, arachnoid, and pia mater), some cerebral spinal fluid, and important vascular structures, such as the superior sagittal sinus. While ultrasound protocols designed to induce vasodilation or to temporally open the blood-brain-barrier conventionally use higher intensities than those employed here, we set out to test the influence of ultrasound on what we shall continue to refer to as the 'meningeal' signal and the gray matter signal. To do this it was obviously necessary to take a somewhat unconventional rs-fMRI analysis approach that did not remove the meningeal signal that is typically regarded as a confound.

A principal component analysis of the signal in the meningeal and gray matter compartments revealed the main components in either compartment explained significantly more variance following TUS compared to control (Fig. 4c; main effect of TUS: $F_{(1,9)}$=30.6, p=0.00036, d=0.67031, CI=[2.1916 5.3343]; in gray matter: $F_{(1,4)}$=10.743, p=0.0306, d=1.3381, CI=[0.47735 5.7655]; in meningeal compartment: $F_{(1,4)}$=16.263, p=0.0157, d=1.6464, CI=[1.3379 72512]). The fact that this effect is present in both compartments could reflect the tight vascular coupling between gray matter and meningeal signal or be driven by partial-voluming effects (these are more pronounced when the size of the brain is relatively small, as for monkey fMRI). This observation suggests that after TUS the BOLD signal became more homogenous. In a seed-based connectivity analysis, as performed here, this would be reflected in a stronger contribution of global signal coupling. However, the impact of TUS presented above do not seem to exhibit this effect, as illustrated by the specificity of the TUS effects for SMA and FPC (Figs. 2, 3), and further underpinned by the absence of TUS effects in regions remote from the stimulation sites (for example, Fig. 4a,d illustrates the case of the

posterior parietal operculum, POp). Importantly, these coupling estimates are obtained when following the conventional rs-fMRI analysis approach to account for global signal confounds by removing WM and meningeal signal contributions before estimating gray matter coupling indices.

We hypothesized that if TUS leads to more homogenous global signal, its contribution to the gray matter signal might have been accounted for when removing meningeal signal components in a linear regression framework[37]. Accordingly, we have repeated the seed-based connectivity analyses after accounting for global signal confounds based on the white matter compartment alone, excluding the meningeal compartment. In these data, global signal contributions were indeed preserved as evidenced by anatomically implausible global connectivity patterns present in the control state (compare panels a and b in Fig. 4, e.g. the prefrontal cortex, encircled). As such, this procedure allowed us to interrogate the global effects of TUS over dorsomedial frontal regions on BOLD signal (see Supplementary Information for full details). Following this procedure, we observed that SMA stimulation appeared to induce widespread increases in signal coupling compared to the control state. This effect was not limited to the stimulation site but also present in remote regions (e.g. when seeded in POp, compare panels b and e in Fig. 4). This effect can be quantified by considering the strength of local connections for every point in the cortex. It is then apparent that the changes induced by stimulation are global in nature (Fig. 4f). In general, when not fully accounting for global confounds, a region's connectivity profile after TUS could be predicted by considering its profile in the control state and adding a spatially flat constant. This suggests an additive non-neuronal source, captured by signal components in the meningeal compartment, may explain the presence and enhancement of global signal observed following TUS over SMA (Fig. 4e,f, e.g. primary sensorimotor cortex)[37]. These effects of TUS on widespread coupling mediated by meningeal signal persisted over time for more than 1 hour after stimulation had ended (Fig. 4g).

Similar effects of TUS on meningeal signal were also observed after FPC TUS (Supplementary Fig. 2). We note that in unconfounded fMRI data FPC TUS did not have a strong impact outside the stimulated region (illustrated for POp in Supplementary Fig. 2). In contrast, in fMRI data confounded by meningeal-driven global nuisance FPC stimulation led to widespread enhanced signal coupling compared to the control state. This effect of FPC TUS was replicated in a new set of animals in experiment 3 (Supplementary Fig. 2). Although the effect was perhaps not as strong as that seen after SMA TUS, this finding again suggests that TUS may produce widespread changes that are non-neuronal in origin. Differences in morphology of the sagittal sinus along the rostro-caudal axis might explain this weakened global effect.

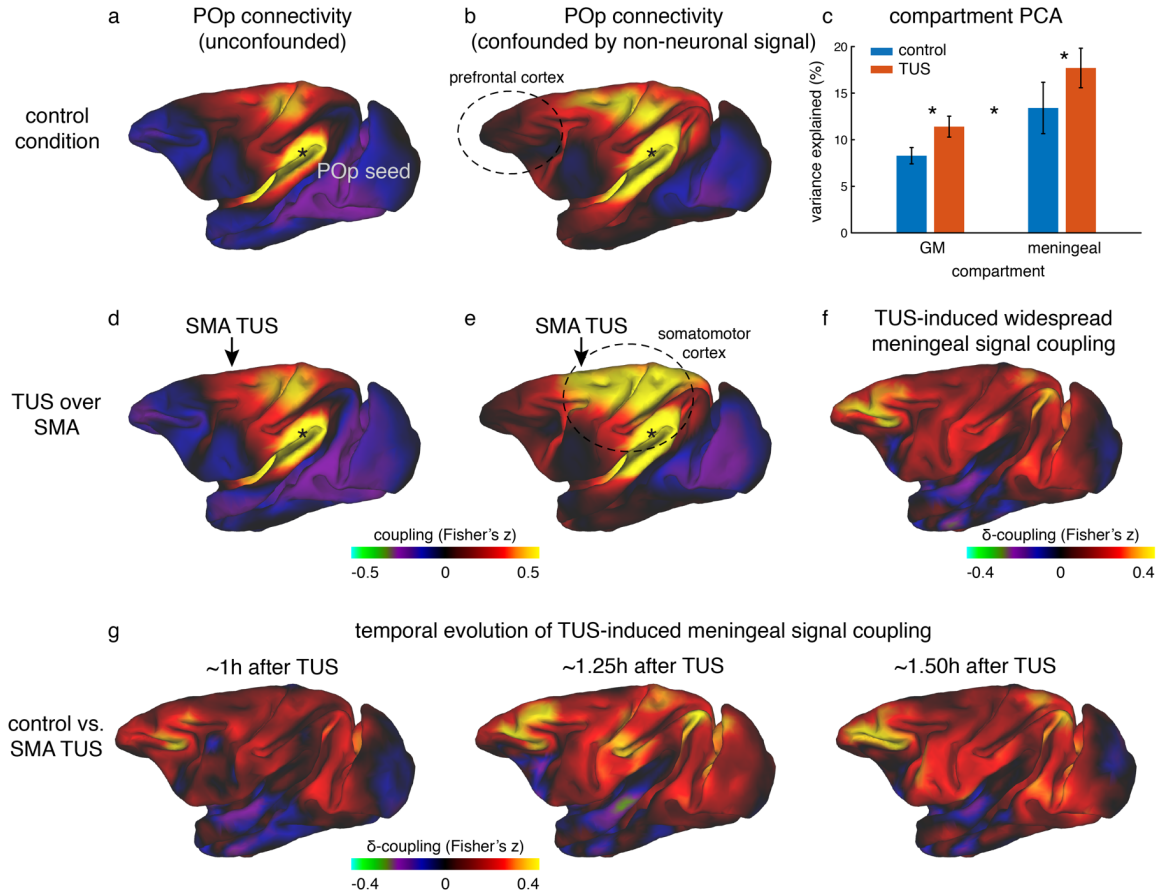

Fig. 4. Non-neuronal signal changes driving widespread coupling. In fully processed fMRI data, unconfounded by global nuisance sources, effects of TUS were not immediately apparent outside the stimulated areas. (**a**,**d**) For example, the whole-brain connectivity pattern of the parietal operculum area (POp, spatially removed from either stimulation site) was unaffected by TUS over SMA. (**b**) When nuisance contributions from the meningeal compartment are not removed (but those from WM are), the presence of globally shared signal is evident: POp is now coupled with that in many other areas. (**e**) POp's global nuisance confounded functional connectivity pattern became stronger after SMA TUS. This was because SMA TUS induced broad changes in BOLD signal even in the meningeal compartment, captured in a principal component analysis (**c**). Error bars denote standard-error of the mean; asterisks denote effects of TUS and WM/meningeal compartment ($p < 0.05$). (**f**) This led to many points in the cortex exhibiting stronger coupling with other brain areas; all areas shown in red are points that have stronger coupling with the rest of the brain after TUS. Note that this effect spread far beyond the stimulation site. (**g**) This widespread TUS-induced meningeal signal coupling persisted over time. All conventions as in Fig. 2 and 3.

Experiment 4

Some higher intensity ultrasound stimulation protocols, distinct from those used here, have been shown to induce thermal lesions or hemorrhage following cavitation[38]. Despite the fact that trains of TUS induced sustained changes in the post-stimulation period in experiments 1 and 2, no structural changes remotely resembling those seen with higher intensity ultrasound protocols. First of all, no tissue alteration (e.g. tissue burn) was observed at the post-mortem examination. Neither were any signs of neuronal alteration or hemorrhage observed in histological analyses of three macaques following pre-SMA TUS (Fig. 5).

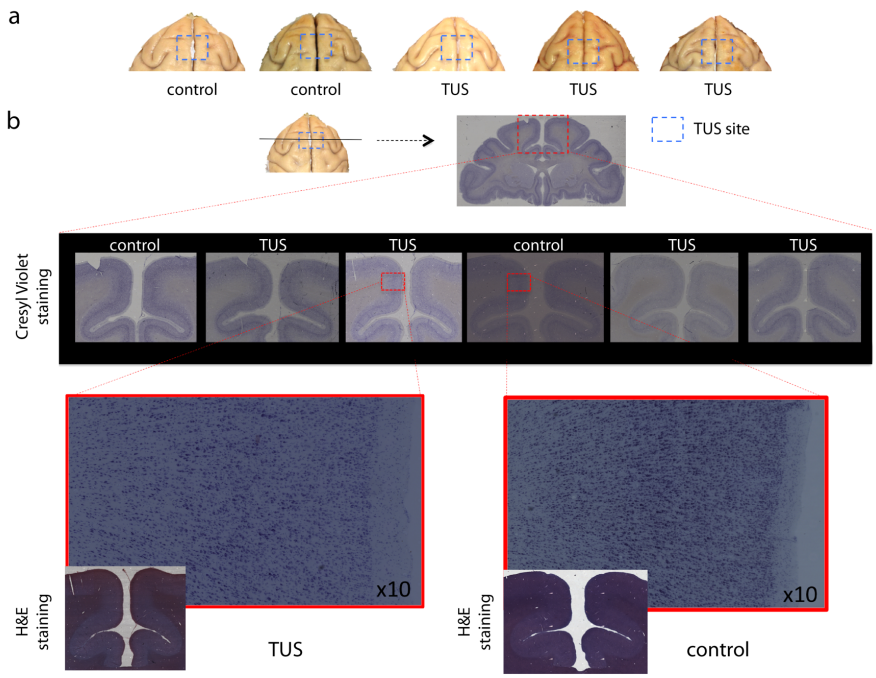

Fig. 5. No effect of TUS was apparent on histological examination. (**a**) Dorsal view of perfused macaque brain. A post-mortem examination of the brain did not reveal macroscopic damage to the brain. (**b**) Histological assessment of 50 micron thick sections obtained at the level of the stimulation site with Cresyl Violet Nissl staining and H&E staining did not reveal any evidence of thermal lesions or hemorrhage after the TUS protocol used here. Magnified images are centered at the focal point of the stimulation, where acoustic energy is expected to be maximal.

Acoustic and thermal modelling

To quantify the pressure amplitude, peak intensities, spatial distribution, and potential temperature changes in the monkey brain associated with the TUS protocol used in this study we simulated the acoustic wave propagation and its thermal effect in a whole head finite element model based on a high-resolution monkey CT scan. As estimated by these numerical simulations, the maximum spatial peak pulse average intensity (I_{sspa}) at the acoustic focus point was 30.7 W/cm^2 for the SMA target and 22.5 W/cm^2 for the FPC target (spatial peak temporal average intensities, I_{spta}: 10.23 W/cm^2 and 7.5 W/cm^2 for SMA and FPC, respectively). Given that the skull is more acoustically absorbing than soft tissue, the highest thermal increase is located in the skull itself, estimated by the simulation to be 2.9°C. Given an approximate 0.5 mm thickness of the dura[39] the maximum temperature below the dura was 38.0°C. The maximal thermal increase at the geometrical focus of the sonic transducer was less than 0.5 °C (Fig. 1g,i).

Discussion

In this study we demonstrate a protocol for transcranial focused ultrasound stimulation (TUS) that can induce a sustained yet reversible change in neural activity. We focused our investigation on modulations of brain connectivity, following the notion that each brain area's unique contribution to cognition and behavior is shaped by how activity in each area is a function of a unique fingerprint of interconnected areas[22]. We found that each area's connectional fingerprint was significantly changed by TUS, but only when it was applied to that area itself (Fig. 2, 3). The changes observed might be summarized as more uniform activation in the stimulated region combined with a sharpening of the normal coupling pattern that each area has even at rest. Activity coupling with strongly interconnected areas, which are often nearby, was increased but activity coupling with less strongly connected regions was reduced. Such changes in connectional fingerprints might constitute the mechanism by which TUS is able to induce regionally specific patterns of behavioral change when applied in awake behaving animals[16,40]. The pattern of inputs each area receives from other areas and the influence it wields over other areas are a major determinant of its function and here we have shown that this pattern is altered by TUS. TUS may therefore provide a relatively straightforward method for sustained but reversible manipulation of specific components of neural circuits in the primate brain[41]. This may be important for investigating primate brain areas when homologues in non-primate species, such as rodents, are non-existent or disputed[42,43]. This work paves the way for the development and use of offline TUS protocols in primates, including humans, both as a research tool and as potential clinical intervention.

In experiments 1 and 2 we found that TUS application produced different effects when applied to different brain regions: the SMA, a part of motor association cortex, and FPC a part of granular prefrontal cortex (Fig. 2, 3). However, in each case the TUS effects were prominent

within the connectional fingerprint of the area stimulated. The connectional fingerprints of SMA and FPC are distinct[28,44,45]. The effects of TUS are thus regionally specific.

Our results confirm that TUS can be used as a neuromodulatory technique that allows one to non-surgically target cortical and subcortical brain areas with superior spatial specificity and depth of stimulation[46], compared to other transcranial stimulation approaches (e.g. TMS and TES)[1–3]. While successes have been achieved with some invasive techniques, such as electrical microstimulation[5,7], it is not easy to use them to disrupt activity in all areas especially when they are not somatopically mapped. Recently it has been reported that some online TUS protocols in rodents induce neural changes as an indirect consequence of the auditory stimulation they entail[17,18]. The spatially specific effects that we observed after TUS cannot, however, be attributed to any common auditory impact that occurs at the time of stimulation. Moreover, in order to avoid both the confounding effect associated with the sound of TUS and interference of the ultrasonic wave field with fMRI measurement, we opted for an 'offline' stimulation protocol. Stimulation was a 40 s train that ended at least 20 minutes before the fMRI data acquisition period. The sustained nature of the train and other features of the stimulation pulses may make the protocol used here more effective for neuromodulation, while ensuring the thermal modulation of the cortex remains limited (< 1 °C, Fig. 1). Such limited thermal changes are not associated neuromodulatory effects observed more than 30 min after the stimulation: the thermal rise is short-lived[11], not accompanied by tissue damage and below the thermal effects observed with some protocols in rodents (for a review, see [47]).

In experiment 3 we found that TUS had reproducible effects. When TUS was applied to FPC in three other individuals, it induced spatially specific effects similar to those seen in experiment 2.

The effects of the non-invasive 40 s stimulation protocol used here are sustained and lasted over much of the two-hour period we investigated. These effects are more extended than those produced by other techniques commonly used for offline disruption of cortical

activity such as TMS[48,49]. Care should therefore be taken in using the technique in human cognitive neuroscience experiments; TUS effects may continue beyond the short periods that participants typically spend within the laboratory. It may therefore be important to carefully characterize the time course of TUS effects in animal models before their use with human participants.

In addition to the spatially specific effects of TUS we also observed changes in the BOLD signal originating from the meningeal compartment that were not specific to the area stimulated. Although similar effects were seen each time either the SMA or FPC was stimulated the effect was generally more pronounced after SMA stimulation than after FPC stimulation. Our preliminary results from TUS of other brain areas suggest that these spatially non-specific effects may be even smaller when TUS is applied elsewhere[46]. While the precise origin of the non-specific effects was difficult to determine it is possible that they may result from a direct vascular effect of TUS; the sagittal sinus is directly above the midline frontal regions that we targeted and is included in the meningeal compartment during MRI analysis protocols. The presence of such non-specific effects again underlines the need for care in translating the technique to human; especially when the targeted region is near venous sinuses or cerebral arteries. In addition, they underline the need for comparing the behavioral effects of TUS not just with a non-stimulation sham condition but with TUS application to another control brain region. The absence of marked histological changes in experiment 4, however, provides one important safety benchmark and confirms previous histological results in lagomorphs[9].

Combining TUS and fMRI is a promising approach to overcome the restrictions of each of the individual techniques. Here we have shown that TUS has a detectable offline and sustained impact on the distinctive network of connectivity associated with the stimulated brain region – the connectional fingerprint. A brain region's interactions with other regions – its unique connectional fingerprint or specific pattern of inputs and outputs – are an important determinant of its functional role. The current results are therefore consistent with

TUS application exerting regionally specific effects on behavior[16,40]. The fact that fMRI allows the effects of TUS to be studied with a high spatial resolution suggests the TUS-fMRI combination has the potential to become a powerful neuroscientific tool.

Acknowledgements

We would like to thank Greg Daubney for his assistance with the histological preparation and analysis, and Dr. Constantin Coussios and Dr. Robin Cleveland for their technical support. Funding for this research was provided by a Wellcome Trust UK Henry Dale fellowship (105651/Z/14/Z), Wellcome Trust Senior Investigator Award (WT100973AIA), Medical Research Council UK (MRC) programme grant (MR/P024955/1), MRC programme grant (G0902373), Wellcome Trust UK Grant (105238/Z/14/Z), Wellcome Trust Sir Henry Wellcome fellowship (103184/Z/13/Z), Biotechnology and Biological Sciences Research Council UK (BBSRC) grant (BB/N019814/1), The Netherlands Organisation for Scientific Research (NWO) grant (452-13-015), The Wellcome Centre for Integrative Neuroimaging (203139/Z/16/Z), Bettencourt Schueller Foundation, and the Agence Nationale de la Recherche under the Future Investments program (ANR-10-EQPX-15).

Author Contributions

PP, JFA, and JS designed the experiment; DF, CC, HA, BA, MS, LR, KK, PP, JFA, and JS acquired the data; LV, CG, DF, CC, DJ, MFSR, JFA, and JS analyzed data; LV, CC, MKF, RBM, and JFA contributed new reagents/analytic tools; SL, KK, MFSR, PP, JFA, and JS provided research resources; LV, CG, DF, KK, MFSR, PP, JFA, and JS wrote the paper.

Declaration of Interests

The authors declare no conflict of interest.

References

1. Bestmann, S. & Walsh, V. Transcranial electrical stimulation. *Curr. Biol.* **27,** R1258–R1262 (2017).
2. Dayan, E., Censor, N., Buch, E. R., Sandrini, M. & Cohen, L. G. Noninvasive brain stimulation: from physiology to network dynamics and back. *Nat. Neurosci.* **16,** 838–844 (2013).
3. Polanía, R., Nitsche, M. A. & Ruff, C. C. Studying and modifying brain function with non-invasive brain stimulation. *Nat. Neurosci.* **21,** 174–187 (2018).
4. Sternson, S. M. & Roth, B. L. Chemogenetic Tools to Interrogate Brain Functions. *Annu. Rev. Neurosci.* **37,** 387–407 (2014).
5. Vanduffel, W. In-Vivo Connectivity in Monkeys. in *Micro-, Meso- and Macro-Connectomics of the Brain* 75–87 (Springer, Cham, 2016). doi:10.1007/978-3-319-27777-6_6
6. Galvan, A., Caiola, M. J. & Albaugh, D. L. Advances in optogenetic and chemogenetic methods to study brain circuits in non-human primates. *J. Neural Transm.* **125,** 547–563 (2018).
7. Krug, K., Salzman, C. D. & Waddell, S. Understanding the brain by controlling neural activity. *Phil Trans R Soc B* **370,** 20140201 (2015).
8. Tufail, Y., Yoshihiro, A., Pati, S., Li, M. M. & Tyler, W. J. Ultrasonic neuromodulation by brain stimulation with transcranial ultrasound. *Nat. Protoc.* **6,** 1453–1470 (2011).

9. Yoo, S.-S. *et al.* Focused ultrasound modulates region-specific brain activity. *NeuroImage* **56,** 1267–1275 (2011).

10. Younan, Y. *et al.* Influence of the pressure field distribution in transcranial ultrasonic neurostimulation. *Med. Phys.* **40,** 082902 (2013).

11. Dallapiazza, R. F. *et al.* Noninvasive neuromodulation and thalamic mapping with low-intensity focused ultrasound. *J. Neurosurg.* **128,** 875–884 (2017).

12. Tyler, W. J., Lani, S. W. & Hwang, G. M. Ultrasonic modulation of neural circuit activity. *Curr. Opin. Neurobiol.* **50,** 222–231 (2018).

13. Kubanek, J., Shukla, P., Das, A., Baccus, S. A. & Goodman, M. B. Ultrasound Elicits Behavioral Responses through Mechanical Effects on Neurons and Ion Channels in a Simple Nervous System. *J. Neurosci.* **38,** 3081–3091 (2018).

14. Kubanek, J. *et al.* Ultrasound modulates ion channel currents. *Sci. Rep.* **6,** 24170 (2016).

15. Prieto, M. L., Oralkan, Ö., Khuri-Yakub, B. T. & Maduke, M. C. Dynamic Response of Model Lipid Membranes to Ultrasonic Radiation Force. *PLoS ONE* **8,** (2013).

16. Deffieux, T. *et al.* Low-Intensity Focused Ultrasound Modulates Monkey Visuomotor Behavior. *Curr. Biol.* **23,** 2430–2433 (2013).

17. Guo, H. *et al.* Ultrasound Produces Extensive Brain Activation via a Cochlear Pathway. *Neuron* (2018). doi:10.1016/j.neuron.2018.04.036

18. Sato, T., Shapiro, M. G. & Tsao, D. Y. Ultrasonic Neuromodulation Causes Widespread Cortical Activation via an Indirect Auditory Mechanism. *Neuron* (2018). doi:10.1016/j.neuron.2018.05.009
19. Airan, R. D. & Pauly, K. B. Hearing out Ultrasound Neuromodulation. *Neuron* **98,** 875–877 (2018).
20. Neubert, F.-X., Mars, R. B., Sallet, J. & Rushworth, M. F. S. Connectivity reveals relationship of brain areas for reward-guided learning and decision making in human and monkey frontal cortex. *Proc. Natl. Acad. Sci.* **112,** E2695–E2704 (2015).
21. O'Reilly, J. X. *et al.* Causal effect of disconnection lesions on interhemispheric functional connectivity in rhesus monkeys. *Proc. Natl. Acad. Sci.* **110,** 13982–13987 (2013).
22. Passingham, R. E., Stephan, K. E. & Kötter, R. The anatomical basis of functional localization in the cortex. *Nat. Rev. Neurosci.* **3,** 606–616 (2002).
23. Caspari, N., Arsenault, J. T., Vandenberghe, R. & Vanduffel, W. Functional Similarity of Medial Superior Parietal Areas for Shift-Selective Attention Signals in Humans and Monkeys. *Cereb. Cortex* **28,** 2085–2099 (2018).
24. Ghahremani, M., Hutchison, R. M., Menon, R. S. & Everling, S. Frontoparietal Functional Connectivity in the Common Marmoset. *Cereb. Cortex* **27,** 3890–3905 (2017).
25. Margulies, D. S. *et al.* Situating the default-mode network along a principal gradient of macroscale cortical organization. *Proc. Natl. Acad. Sci.* **113,** 12574–12579 (2016).

26. Margulies, D. S. *et al.* Precuneus shares intrinsic functional architecture in humans and monkeys. *Proc. Natl. Acad. Sci.* **106,** 20069–20074 (2009).

27. Mars, R. B., Sallet, J., Neubert, F.-X. & Rushworth, M. F. S. Connectivity profiles reveal the relationship between brain areas for social cognition in human and monkey temporoparietal cortex. *Proc. Natl. Acad. Sci.* **110,** 10806–10811 (2013).

28. Sallet, J. *et al.* The Organization of Dorsal Frontal Cortex in Humans and Macaques. *J. Neurosci.* **33,** 12255–12274 (2013).

29. Shen, H. H. Core Concept: Resting-state connectivity. *Proc. Natl. Acad. Sci.* **112,** 14115–14116 (2015).

30. Shen, K., Hutchison, R. M., Bezgin, G., Everling, S. & McIntosh, A. R. Network Structure Shapes Spontaneous Functional Connectivity Dynamics. *J. Neurosci.* **35,** 5579–5588 (2015).

31. Petrides, M. & Pandya, D. N. Efferent Association Pathways from the Rostral Prefrontal Cortex in the Macaque Monkey. *J. Neurosci.* **27,** 11573–11586 (2007).

32. Dum, R. P. & Strick, P. L. Frontal Lobe Inputs to the Digit Representations of the Motor Areas on the Lateral Surface of the Hemisphere. *J. Neurosci.* **25,** 1375–1386 (2005).

33. Geyer, S., Matelli, M., Luppino, G. & Zilles, K. Functional neuroanatomy of the primate isocortical motor system. *Anat. Embryol. (Berl.)* **202,** 443–474 (2000).

34. Strick, P. L., Dum, R. P. & Picard, N. Motor areas on the medial wall of the hemisphere. *Novartis Found. Symp.* **218,** 64–75; discussion 75-80, 104–108 (1998).

35. Bates, J. F. & Goldman-Rakic, P. S. Prefrontal connections of medial motor areas in the rhesus monkey. *J. Comp. Neurol.* **336,** 211–228 (1993).

36. Lu, M.-T., Preston, J. B. & Strick, P. L. Interconnections between the prefrontal cortex and the premotor areas in the frontal lobe. *J. Comp. Neurol.* **341,** 375–392 (1994).

37. Verhagen, L. How to grasp a ripe tomato. (Utrecht University; Donders Institute, Radboud University, 2012).

38. Elias, W. J. *et al.* A magnetic resonance imaging, histological, and dose modeling comparison of focused ultrasound, radiofrequency, and Gamma Knife radiosurgery lesions in swine thalamus. *J. Neurosurg.* **119,** 307–317 (2013).

39. Galashan, F. O. *et al.* A new type of recording chamber with an easy-to-exchange microdrive array for chronic recordings in macaque monkeys. *J. Neurophysiol.* **105,** 3092–3105 (2011).

40. Fouragnan, E. *et al.* The macaque anterior cingulate cortex translates counterfactual choice value into actual behavioral change. *bioRxiv* (2018). doi:10.1101/342303

41. Wattiez, N. *et al.* Transcranial ultrasonic stimulation modulates single-neuron discharge in macaques performing an antisaccade task. *Brain Stimulat.* **10,** 1024–1031 (2017).

42. Preuss, T. M. Do rats have prefrontal cortex? The rose-woolsey-akert program reconsidered. *J. Cogn. Neurosci.* **7,** 1–24 (1995).

43. Wise, S. P. Forward frontal fields: phylogeny and fundamental function. *Trends Neurosci.* **31,** 599–608 (2008).

44. Johansen-Berg, H. *et al.* Changes in connectivity profiles define functionally distinct regions in human medial frontal cortex. *Proc. Natl. Acad. Sci.* **101,** 13335–13340 (2004).

45. Neubert, F.-X., Mars, R. B., Thomas, A. G., Sallet, J. & Rushworth, M. F. S. Comparison of Human Ventral Frontal Cortex Areas for Cognitive Control and Language with Areas in Monkey Frontal Cortex. *Neuron* **81,** 700–713 (2014).

46. Folloni, D. *et al.* Manipulation of activity in deep structures of the primate brain using transcranial fo-cused ultrasound stimulation. *bioRxiv* (2018). doi:10.1101/336917

47. Constans, C., Mateo, P., Tanter, M. & Aubry, J.-F. Potential impact of thermal effects during ultrasonic neurostimulation: retrospective numerical estimation of temperature elevation in seven rodent setups. *Phys. Med. Biol.* **63,** 025003 (2018).

48. Huang, Y.-Z., Edwards, M. J., Rounis, E., Bhatia, K. P. & Rothwell, J. C. Theta Burst Stimulation of the Human Motor Cortex. *Neuron* **45,** 201–206 (2005).

49. O'Shea, J., Johansen-Berg, H., Trief, D., Göbel, S. & Rushworth, M. F. S. Functionally Specific Reorganization in Human Premotor Cortex. *Neuron* **54,** 479–490 (2007).

50. Constans, C., Deffieux, T., Pouget, P., Tanter, M. & Aubry, J. F. A 200-1380-kHz Quadrifrequency Focused Ultrasound Transducer for Neurostimulation in Rodents and Primates: Transcranial In Vitro Calibration and Numerical Study of the Influence of Skull Cavity. *IEEE Trans. Ultrason. Ferroelectr. Freq. Control* **64,** 717–724 (2017).

Supplementary Information

Subject details

For this study, six healthy male macaques (*Macaca mulatta*) were stimulated with transcranial focused ultrasound and scanned to acquire resting state functional magnetic resonance (rs-fMRI) and anatomical MR images. Three animals participated in experiments 1 and 2, including the control condition (all males, mean age and weight at time of scan: control, 5.5 years, 10.2 kg; SMA TUS, 5.6 years, 10.7 kg; FPC TUS, 6.1 years, 11.8 kg). Three different animals participated in experiment 3 (all males, mean age and weight at time of scan: 10.3 years, 13 kg). In addition to this set of animals, six animals were included in the histology analysis (experiment 4): three control animals who did not receive TUS (2 females; mean age and weight at time of perfusion: 9.3 years, 9.1 kg) and three pre-SMA TUS animals post stimulation (all males; mean age and weight at time of perfusion: 8.4 years, 13.1 kg).

All procedures were conducted under licenses from the United Kingdom (UK) Home Office in accordance with The Animals (Scientific Procedures) Act 1986. In all cases they complied with the European Union guidelines (EU Directive 2010/63/EU).

Ultrasound stimulation

A single element ultrasound transducer (H115-MR, diameter 64 mm, Sonic Concept, Bothell, WA, USA) with 51.74 mm focal depth was used with a coupling cone filled with degassed water and sealed with a latex membrane (Durex). The resonance frequency of ultrasonic wave was set at 250 kHz with 30 ms bursts of ultrasound generated every 100 ms, controlled through a digital function generator (Handyscope HS5, TiePie engineering, Sneek, The Netherlands). The stimulation lasted for 40 seconds. A 75-Watt amplifier (75A250A, Amplifier Research, Souderton, PA) was used to deliver the required power to the transducer. A TiePie probe (Handyscope HS5, TiePie engineering, Sneek, The Netherlands) connected to an oscilloscope was used to monitor the voltage delivered. The recorded peak-to-peak voltage

was kept constant throughout the stimulation. Voltage values per session ranged from 130 to 142 V, corresponding to 1.17 to 1.35 MPa as measured in water with an in house heterodyne interferometer interferometer[50]. Based on numerical simulations (see *Acoustic and thermal modelling* below for more details), the maximum peak pressure (P_{max}) and I_{sspa} at the acoustic focus point were estimated to be 0.99 MPa and 30.7 W/cm^2 for the SMA target, and 0.85 MPa and 22.5 W/cm^2 for the FPC target (I_{spta}: 10.23 W/cm^2 and 7.5 W/cm^2 for SMA and FPC, respectively). Each of the areas targeted in experiments 1-4 lie close to the midline. Therefore, we applied a single train over the midline stimulating the target region in both hemispheres simultaneously.

In order to direct TUS to the target region, we guided the stimulation using a frameless stereotaxic neuronavigation system (Rogue Research, Montreal, CA) set up for each animal individually by registering a T1-weighted MR image to the animal's head. Positions of both the ultrasound transducer and the head of the animal were tracked continuously with infrared reflectors to inform online and accurate positioning of the transducer over the targeted brain region: SMA in experiment 1, (Montreal Neurological Institute (MNI) X, Y, and Z coordinates in mm [0.1 2 19]); FPC in experiment 2 [0.6 24 10]; FPC in experiment 3 [-0.7 24 11]; pre-SMA in experiment 4 [0.2 11 17]. The ultrasound transducer / coupling cone montage was placed directly onto previously shaved skin prepared with conductive gel (SignaGel Electrode; Parker Laboratories Inc.) to ensure ultrasonic coupling between the transducer and the animal's scalp. In the non-stimulation condition (control), all procedures (anesthesia, pre-scan preparation, fMRI scan acquisition and timing), with the exception of actual TUS, matched the TUS sessions.

Acoustic and thermal modelling

The acoustic wave propagation of our focused ultrasound protocol (at 130 V peak-to-peak voltage) was simulated using a k-space pseudospectral method-based solver, k-Wave[51] to obtain estimates for the pressure amplitude, peak intensity, spatial distribution, and thermal

impact at steady state. 3D maps of the skull were extracted from a monkey CT scan (Kyoto University online database, ID 1478, 0.26 mm isotropic resolution). Soft tissues were assumed to be homogeneous, with acoustic values of water (ρ_{tissue} =1000 kg/m3 and c_{tissue} =1500 m/s). In the bone, a linear relationship between the Hounsfield Units (HU) from the CT scan and the sound speed, as well as the density, was used. The power law model for attenuation is $\alpha_{att} = \alpha_1 * \Phi^{\beta}$ where the porosity Φ is defined by $\Phi = \frac{\rho_{max}-\rho}{\rho_{max}-\rho_{water}}$ in the skull[52]. The attenuation coefficient for the acoustic propagation α1 depends on the frequency: $\alpha_1 = \alpha_0 f^b$. We set the parameters to $\rho_{max} = 2200\ \mathrm{kg}/m^3, c_{max} = 3100\ m/s, \beta = 0.5, \alpha_0 = 8\ dB/cm/MHz^b$, b=1.1[47]. The attenuation coefficient in bone accounts for both absorption and scattering.

The propagation simulation was performed at 250 kHz with a 150µs-long pulse signal (enough to reach a steady state). The transducer was modelled as a spherical section (63 mm radius of curvature and 64 mm active diameter). The simulated pulses were spatially apodized (r = 0.35) on the spherical section. Ultrasound propagates first through water before entering the skull cavity with the geometrical focal point located below the surface, inside the brain. Simulations were performed in free water, and the maximum amplitude obtained was used to rescale the results in skull (the transducer calibration indicates that the maximum amplitude in water at 130V is 1.2 MPa). The thermal modeling is based on the bio-heat equation[53]:

$$\rho C \frac{\partial T}{\partial t} = \kappa \nabla^2 T + q + w \rho_b C_b (T - T_a)$$

where T, ρ, C, κ and q are the temperature, density, specific heat, thermal conductivity and rate of heat production respectively. Heat production is defined as $q = \alpha_{abs} \frac{P^2}{2\rho C}$, α_{abs} being the absorption coefficient and P the peak negative pressure. κ is set to 0.528 $W.m^{-1}.K^{-1}$ in soft tissue and 0.4 $W.m^{-1}.K^{-1}$ in the skull; C is set to 3600 $J.kg^{-1}.K^{-1}$ in soft tissue and 1300 $J.kg^{-1}.K^{-1}$ in the skull[54]. In the tissue, the absorption coefficient was set to $\alpha_{abs\ tissue} = 0.21\ \mathrm{dB/cm}/MHz^b$ [55]. In the skull the longitudinal absorption coefficient is proportional to

the density with $\alpha_{\text{abs max}}=\alpha_0/3$ = 2.7 dB/cm/MHz^b [56]. The last term corresponds to the perfusion process: w, ρ_b, C_b and T_a correspond to the blood perfusion rate, blood density, blood specific heat and blood ambient temperature respectively. These parameters are assumed homogeneous over the brain, although a more detailed description of the brain cooling processes can be found in the literature[57]. The perfusion parameters are based on previous reports[58]: w=0.008s^{-1}; ρ_b= 1030 kg.m^{-3}; C_b = 3620 J.kg^{-1}.K^{-1} and T_a = 37°C.

The bioheat equation is solved by using a 3D finite-difference scheme in MATLAB (Mathworks, Natick, USA) with Dirichlet boundary conditions. Initial temperature conditions were 37°C in the brain, skull and tissue, and 24°C in the water coupling cone. Simulations were run over 1 minute pre-sonication, followed by 40 s of sonication, and 5 minutes post-sonication, closely following the experimental procedure.

Macaque MRI acquisition

MRI scans were collected under inhalational isoflurane gas anesthesia using a protocol which has previously proven successful in preserving whole-brain functional connectivity as measured with BOLD signal[20,21,27,28,45,59,60]. In the case of the TUS conditions, fMRI data collection began only after completion of the TUS train. Anesthesia was induced using intramuscular injection of ketamine (10 mg/kg), xylazine (0.125– 0.25 mg/kg), and midazolam (0.1 mg/kg). Macaques also received injections of atropine (0.05 mg/kg, intramuscularly), meloxicam (0.2 mg/kg, intravenously), and ranitidine (0.05 mg/kg, intravenously). The anesthetized animals were placed in an MRI-compatible frame (Crist Instruments) in a sphinx position and placed in a horizontal 3 T MRI scanner with a full-size bore. Scanning commenced ~2 h after induction, when the clinical peak of ketamine had passed. Anesthesia was maintained, in accordance with veterinary recommendation, using the lowest possible concentration of isoflurane to ensure that macaques were anesthetized. The depth of anesthesia was assessed and monitored using physiological parameters (heart rate and blood pressure, as well as clinical checks before the scan for muscle relaxation). During the

acquisition of the functional data the expired isoflurane concentration was in the range 0.6-0.8%. Isoflurane was selected for the scans as it was previously demonstrated to preserve rs-fMRI networks[20,21,27,28,45,59,60]. Macaques were maintained with intermittent positive pressure ventilation to ensure a constant respiration rate during the functional scan, and respiration rate, inspired and expired CO2, and inspired and expired isoflurane concentration were monitored and recorded using VitalMonitor software (Vetronic Services Ltd.). Core temperature and SpO2 were also constantly monitored throughout the scan. A four-channel phased-array coil was used for data acquisition (Dr. H. Kolster, Windmiller Kolster Scientific, Fresno, CA, USA).

FMRI data were collected in experiments 1-3. Whole-brain BOLD fMRI data were collected from each animal for 3 runs of approximately 26 minutes each, using the following parameters: 36 axial slices; in-plane resolution, 2 x 2 mm; slice thickness, 2 mm; no slice gap; TR, 2000 ms; TE, 19 ms; 800 volumes per run. A minimum period of 10 days elapsed between sessions.

T1-weighted structural MRI scans were collected in experiments 1-3. A structural scan (average over up to three T1w images acquired in the same session) was acquired for each macaque in the same session, using a T1 weighted magnetization-prepared rapid-acquisition gradient echo sequence (0.5 x 0.5 x 0.5 mm voxel resolution).

Macaque anatomical MRI preprocessing

The preprocessing and analysis of the MRI data was designed to follow the HCP Minimal Processing Pipeline[61], using tools of FSL (https://fsl.fmrib.ox.ac.uk/fsl/fslwiki), HCP Workbench (https://www.humanconnectome.org/software/connectome-workbench), and the Magnetic Resonance Comparative Anatomy Toolbox (MrCat; http://www.rbmars.dds.nl/lab/toolbox.html). The T1w images were processed in an iterative fashion cycling through brain-extraction, RF bias-field correction, and linear and non-linear template registration to the *macaca mulatta* F99 atlas[62]. The initial skull stripping was

performed using a multi-seeded implementation of BET[63] optimized for macaque brains, while subsequent brain extraction was based on a high-fidelity template registered to the F99 macaque space. The RF bias-field was estimated and corrected using a robust implementation of FAST[64]. Linear and non-linear registration to F99 space was achieved using FLIRT[65,66] and FNIRT[67,68] with configurations adjusted to reflect macaque rather than human brain characteristics. The application of a robust and macaque-optimised version of FAST also resulted in compartments estimated for grey matter, white matter, and meninges with cerebral spinal fluid. For each compartment a posterior-probability map was created by integrating a set of prior probability maps based on 112 *Macaca mullata* individuals[69] with the dataset-specific evidence provided by FAST. Segmentation of subcortical structures was achieved by registration to the D99 atlas[70].

Macaque rs-fMRI preprocessing

The first 5 volumes of the functional EPI datasets were discarded to ensure a steady RF excitation state. EPI timeseries were motion corrected using MCFLIRT. Given that the animals were anesthetized and their heads were held in a steady position, any apparent image motion, if present at all, is caused by changes to the B0 field, rather than by head motion. Accordingly, the parameter estimates from MCFLIRT can be considered to be 'B0-confound parameters' instead. Each timeseries was checked rigorously for spikes and other artefacts, both visually and using automated algorithms; where applicable slices with spikes were linearly interpolated based on temporally neighboring slices. Brain extraction, bias-correction, and registration was achieved for the functional EPI datasets in an iterative manner, similar to the preprocessing of the structural images with the only difference that the mean of each functional dataset was registered to its corresponding T1w image using rigid-body boundary-based registration (FLIRT). EPI signal noise was reduced both in the frequency and temporal domain. The functional time series were high-pass filtered with a frequency cut-off at 2000 seconds. Temporally cyclical noise, for example originating from the

respiration apparatus, was removed using band-stop filters set dynamically to noise peaks in the frequency domain of the first three principal components of the timeseries.

To account for remaining global signal confounds we considered the signal timeseries in white matter (WM) and meningeal compartments. Specifically, the WM+meningeal confound timeseries was described by the mean time course and the first five subsequent principal components of the combined WM and meningeal compartment (considering only voxels with a high posterior probability of belonging to the WM or meningeal compartment, obtained in the T1w image using FAST). The principal components of the WM+meningeal signal were estimated using a singular value decomposition approach. The B0 confound parameter estimates obtained from MCFLIRT were expanded as a second degree Volterra series to capture both linear and non-linear B0 effects. Together the WM+meningeal and expanded B0 confound parameters were regressed out of the BOLD signal for each voxel.

In a separate analysis (Fig. 4 and Supplementary Fig. 2), to assess the contribution of the meningeal compartment signal we repeated the identical procedure as above, with the only difference that the mean and principal components were extracted from signal in the WM compartment alone, excluding the meningeal compartment.

Following this confound cleaning step, the time course was low-pass filtered with a cut-off at 10 seconds. The cleaned and filtered signal was projected from the conventional volumetric representation (2 mm voxels) to the F99 cortical surface (~1.4 mm spaced vertices), while maintaining the subcortical volumetric structures. The data were spatially smoothed using a 3 mm FWHM gaussian kernel, taking into account the folding of the cortex and the anatomical boundaries of the subcortical structures. Lastly, the data timeseries were demeaned to prepare for functional connectivity analyses.

To represent subject effects, the timeseries from the three runs were concatenated to create a single timeseries per animal per intervention (control, SMA TUS, FPC TUS). To represent group effects the run-concatenated timeseries of all animals were combined using a group-PCA approach[71] that was set to reduce the dimensionality of the data.

Macaque rs-fMRI analyses

To construct regions-of-interest (ROI) for SMA and FPC circles of 4 mm radius were drawn on the cortical surface around the point closest to the average stimulation coordinate (Fig. 1), in both the left and the right hemisphere. The same procedure was used to define other bilateral cortical regions of interest, based on literature coordinates[20,28,45,60], to serve as seeds for connectivity analyses (POp, Fig. 4, Supplementary Fig. 2) or targets for the fingerprint analyses (Fig. 3). Apart from the stimulation sites and primary auditory cortex, all ROIs were selected based on their known anatomical connectivity, of relevance because they are known to be distinctively strongly or distinctively weakly connected with the stimulation sites.

Coupling between the activity of each region of interest and the rest of the brain was estimated by calculating the correlation coefficient between each point in the ROI and all other data points (Fisher's *z*: inverse hyperbolic tangent of Pearson's *r*, bounded at [-2 2]). The resulting 'connectivity-maps' were averaged across all vertices/voxels in the ROI, and subsequently averaged across hemispheres. Accordingly, the final maps represent the average coupling of a bilateral ROI with the rest of the brain. The fingerprints are obtained by extracting the average coupling with each target ROI and averaging across the two hemispheres.

The strength of self-connections within SMA and FPC ROIs was estimated in the same way as the coupling of either SMA or FPC with any remote ROI was determined. Namely, for each point in the ROI the Fisher's *z*-transformed correlation between this point's timeseries and that of each of the other points in the ROI was calculated. Subsequently, for each point the resultant *z*-values were averaged, describing local coupling at that point, and averaged across the whole ROI to obtain a single estimate of self-coupling per ROI (Fig. 3c).

To assess the contribution of the meningeal compartment signal, we quantified the effect of TUS for each point on the cortical surface in data that was not corrected for the meningeal signal (see *Macaque rs-fMRI preprocessing*). For each point, we calculated it's

coupling with the rest of the brain, sorted all Fisher's *z*-values in ascending order, and extracted the *z*-value at the 98th-percentile. *Z*-values at this level describe relatively strong coupling with the seed point and are often observed in the vicinity of the seed region or other strongly connected regions (depicted in bright yellow in Fig. 4), ensuring that irrelevant connections are ignored. As such, this simple statistic is well-suited to capture any main effects of TUS on coupling strength, including those observed when comparing panels (b) and (e) in Fig. 4. This statistic allows us to quantify the effect of TUS in a single value for each point on the cortical surface, and to directly contrast the values obtained in the control state with those obtained after TUS (Fig. 4f, Supplementary Fig. 2f,i).

We described the signal variance in the GM and meningeal compartments, or more specifically, the variance explained by the first five principal components (Fig. 4c, Supplementary Fig. 2c), using the same approach that was used to decompose signal in WM or WM+meningeal compartments in the EPI timeseries cleaning step, as described above. We defined the explained variance as the sum of the first five eigenvalues of the covariance matrix of the compartment signals divided by the sum of all eigenvalues.

Statistics

Randomization was used in all experiments. Data collection and analysis were not performed blind to the conditions of the experiments. No data was excluded for analysis. In the absence of relevant reports of expected effect size the sample sizes could not be predetermined statistically but were similar to those reported in previous publications detailing (interventional) macaque fMRI studies[21,72,73]. Statistical inference on the fingerprints was performed using one-sided non-parametric permutation tests on cosine similarity metrics describing the similarity of the shape of the fingerprints irrespective of their mean[74]. In contrast to conventional parametric tests, this approach does not rely on assumptions about the shape of the distribution but will acknowledge dependencies between target ROIs in the fingerprint; as such this approach will avoid inflation of type I error. The relatively small

number of TUS sites, animals, and fMRI runs allowed us to exhaustively test all possible permutations (24309) to obtain the true probability of rejecting the null hypothesis.

All other statistical inferences were drawn in the context of generalized linear mixed-effects (GLME) models that considered the intercept and factorial design (including interactions where appropriate) as fixed effects and the intercept and slope grouped per animal as random effects with possible correlation between them (as implemented in MATLAB, Mathworks, Natick, USA). The models were assumed to adhere to a normal distribution of the data (not formally tested) and were fitted using Maximum-Pseudo-Likelihood estimation methods where the covariance of the random effects was approximated using Cholesky parameterization. Statistical significance was set at $\alpha = 0.05$, two-tailed, and estimated using conventional analyses of variance (ANOVA). For all parametric tests we report the test statistic (*F*), probability estimate (*p*), effect size (Cohen's *d*), and the lower and upper limits of the 95 % confidence interval (CI). For all plots, the central tendency across individual animals is derived directly from the group-PCA approach[71] or described as the mean across all animals (n=3). Dispersion is described as the standard-error of the mean (SE).

Histology

In experiment 4, prior to histological examination, animals were anesthetized with sodium pentorbarbitone and perfused with 90% saline and 10% formalin. A post-mortem examination of the surface of the brain was conducted prior to the brain extraction. The brains were then removed and placed in 10% sucrose formalin. The brains were blocked in the coronal plane at the level of the lunate sulcus. Each brain was cut in 50-µm coronal sections. Every tenth section, two adjacent sections were retained for analysis whereby one was stained with Cresyl Violet (Nissl body staining) and the other with Haemotoxylin and Eosin (H&E staining).

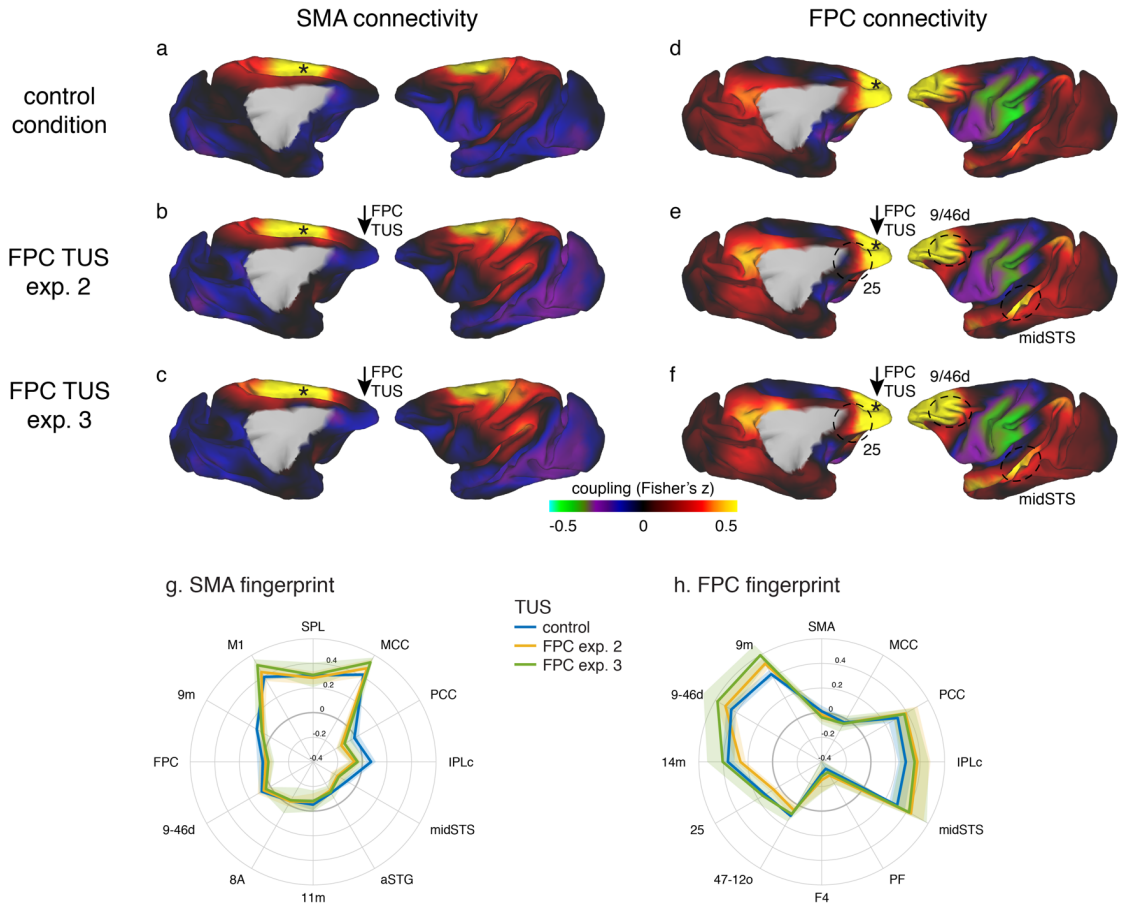

Supplementary Fig. 1. Specific patterns of change in the coupling of activity between stimulated areas and the rest of the brain were replicated in experiments 2 and 3. Panels on the left show activity coupling between SMA and the rest of the brain in control animals (**a**), after FPC TUS in experiment 2 (**b**), and after FPC TUS in experiment 3 (**c**). Panels on the right show activity coupling between FPC and the rest of the brain in control animals (**d**), after FPC TUS in experiment 2 (**e**), and after FPC TUS in experiment 3 (**f**). SMA's connectional fingerprint was largely unaltered after FPC TUS in both experiments 2 and 3 (**g**) but FPC's connectivity fingerprint was altered in a similar manner in both experiments 2 and 3 (**h**). Panels (a, b) and (d, e) are reproduced here from Fig. 2 for comparison. All conventions as in Fig. 2. Lighter colored error bands indicate the standard-error of the mean across individual animals.

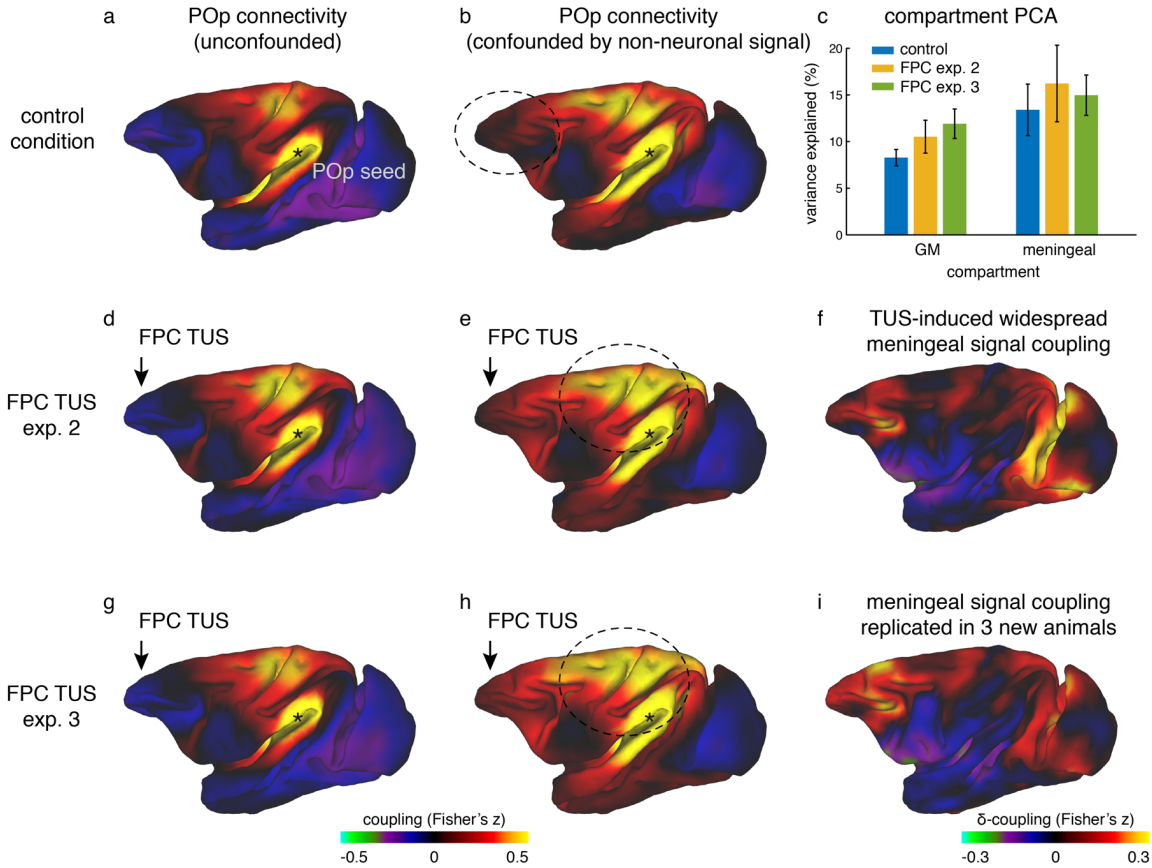

Supplementary Fig. 2. Widespread non-neuronal signal changes were replicated in experiments 2 and 3. (**a**) Whole-brain connectivity pattern of area POp, a region removed from the stimulation sites, in the control state without TUS. (**d**) This region's connectivity is unaffected by TUS over FPC, confirming the absence of remote effects following SMA TUS in experiment 1 (Fig. 4). (**g**) The relative absence of remote effects (illustrated by POp) following FPC TUS in experiment 2 is replicated in experiment 3 in a new set of 3 animals. (**b**) When signal in the meningeal compartment is not considered in the noise estimation step POp's connectivity is confounded by global nuisance signal. (**e**) Similar to the effects observed after SMA TUS, POp's global nuisance confounded functional connectivity pattern became stronger after FPC TUS. (**c**) This was because FPC TUS induced broad changes in BOLD signal even in the meningeal compartment, captured in a principal component analysis, both in experiments 2 and 3. Error bars denote standard-error of the mean. (**f**) This led to many points in the cortex exhibiting stronger coupling with other brain areas; all areas shown in red are points that have stronger coupling with the rest of the brain after TUS. (**h**,**i**) This widespread meningeal signal coupling following FPC TUS and its effect on POp's connectivity pattern was replicated in experiment 3. Panels (**a**) and (**b**) are reproduced here from Fig. 4 for comparison. All conventions as in Fig. 4.

Supplementary References

51. Cox, B. T., Kara, S., Arridge, S. R. & Beard, P. C. k-space propagation models for acoustically heterogeneous media: Application to biomedical photoacoustics. *J. Acoust. Soc. Am.* **121,** 3453–3464 (2007).
52. Aubry, J.-F., Tanter, M., Pernot, M., Thomas, J.-L. & Fink, M. Experimental demonstration of noninvasive transskull adaptive focusing based on prior computed tomography scans. *J. Acoust. Soc. Am.* **113,** 84–93 (2003).
53. Pennes, H. H. Analysis of Tissue and Arterial Blood Temperatures in the Resting Human Forearm. *J. Appl. Physiol.* **1,** 93–122 (1948).
54. Duck, F. A. *Physical Properties of Tissues: A Comprehensive Reference Book*. (Academic Press, 2013).
55. Goss, S. A., Frizzell, L. A. & Dunn, F. Ultrasonic absorption and attenuation in mammalian tissues. *Ultrasound Med. Biol.* **5,** 181–186 (1979).
56. Pinton, G. *et al.* Attenuation, scattering, and absorption of ultrasound in the skull bone. *Med. Phys.* **39,** 299–307 (2012).
57. Wang, H., Kim, M., Normoyle, K. P. & Llano, D. Thermal Regulation of the Brain—An Anatomical and Physiological Review for Clinical Neuroscientists. *Front. Neurosci.* **9,** (2016).

58. Pulkkinen, A., Huang, Y., Song, J. & Hynynen, K. Simulations and measurements of transcranial low-frequency ultrasound therapy: skull-base heating and effective area of treatment. *Phys. Med. Biol.* **56,** 4661 (2011).

59. Vincent, J. L. *et al.* Intrinsic functional architecture in the anaesthetized monkey brain. *Nature* **447,** 83–86 (2007).

60. Mars, R. B. *et al.* Diffusion-Weighted Imaging Tractography-Based Parcellation of the Human Parietal Cortex and Comparison with Human and Macaque Resting-State Functional Connectivity. *J. Neurosci.* **31,** 4087–4100 (2011).

61. Glasser, M. F. *et al.* The minimal preprocessing pipelines for the Human Connectome Project. *NeuroImage* **80,** 105–124 (2013).

62. Van Essen, D. C. & Dierker, D. L. Surface-Based and Probabilistic Atlases of Primate Cerebral Cortex. *Neuron* **56,** 209–225 (2007).

63. Smith, S. M. Fast robust automated brain extraction. *Hum. Brain Mapp.* **17,** 143–155 (2002).

64. Zhang, Y., Brady, M. & Smith, S. Segmentation of brain MR images through a hidden Markov random field model and the expectation-maximization algorithm. *IEEE Trans. Med. Imaging* **20,** 45–57 (2001).

65. Jenkinson, M., Bannister, P., Brady, M. & Smith, S. Improved Optimization for the Robust and Accurate Linear Registration and Motion Correction of Brain Images. *NeuroImage* **17,** 825–841 (2002).

66. Jenkinson, M. & Smith, S. A global optimisation method for robust affine registration of brain images. *Med. Image Anal.* **5,** 143–156 (2001).

67. Andersson, J. L. R., Jenkinson, M. & Smith, S. Non-linear registration aka Spatial normalisation - FMRIB Technial Report TR07JA2. (2007).

68. Jenkinson, M., Beckmann, C. F., Behrens, T. E. J., Woolrich, M. W. & Smith, S. M. FSL. *NeuroImage* **62,** 782–790 (2012).

69. McLaren, D. G. *et al.* A population-average MRI-based atlas collection of the rhesus macaque. *NeuroImage* **45,** 52–59 (2009).

70. Reveley, C. *et al.* Three-Dimensional Digital Template Atlas of the Macaque Brain. *Cereb. Cortex* **27,** 4463–4477 (2017).

71. Smith, S. M., Hyvärinen, A., Varoquaux, G., Miller, K. L. & Beckmann, C. F. Group-PCA for very large fMRI datasets. *NeuroImage* **101,** 738–749 (2014).

72. Chau, B. K. H. *et al.* Contrasting Roles for Orbitofrontal Cortex and Amygdala in Credit Assignment and Learning in Macaques. *Neuron* **87,** 1106–1118 (2015).

73. Papageorgiou, G. K. *et al.* Inverted activity patterns in ventromedial prefrontal cortex during value-guided decision-making in a less-is-more task. *Nat. Commun.* **8,** 1886 (2017).

74. Mars, R. B. *et al.* Comparing brains by matching connectivity profiles. *Neurosci. Biobehav. Rev.* **60,** 90–97 (2016).